DOI 10.1007/s10946-022-10054-1
Journal of Russian Laser Research, Volume 43, Number 3, May, 2022

HIGH-SENSITIVITY TEMPERATURE SENSOR BASED ON TWO PARALLEL FABRY–PÉROT INTERFEROMETERS AND VERNIER EFFECT

Shiyi Zhang, Chao Jiang,* Jie Ren, Hailin Chen, Jiao Song, Xiaoshan Guo, and Simei Sun

College of Physics and Electronic Science, Hubei Normal University
Huangshi, Hubei 435002, China

*Corresponding author e-mail: jiangchao1969@hbnu.edu.cn

Abstract

We propose a novel sensor with its temperature sensitivity improved by the Vernier effect. The sensor comprises two parallel Fabry–Pérot interferometers (FPI), namely, FPI_1 and FPI_2, which have a similar free spectral range (FSR) to obtain the Vernier effect. FPI_1 and FPI_2 are formed by a single-mode fiber inserted into a ceramic ferrule and an UV-curable glue film on the end surface of the ceramic ferrule. Since the UV-curable glue is a thermally sensitive material, FPI_1 is very sensitive to temperature. The experimental results show that the temperature sensitivity of the proposed sensor is up to −14.633 nm/°C, which is 9.6 times that of the single FPI_1 temperature sensor (1.5271 nm/°C). The sensor elaborated has a simple structure, good repeatability, high sensitivity, and low cost. It can be easily fabricated and has broad application prospects.

Keywords: fiber-optic sensor, Fabry–Pérot interferometer, ceramic ferrule, ultraviolet-curable glue, temperature sensor.

1. Introduction

Optical-fiber temperature sensors have been deeply studied due to their passive operation, easy manufacturing process, remote sensing capability, and anti-electromagnetic interference performance. There are two main types of optical-fiber temperature sensors, namely, optical-fiber grating temperature sensors [1, 2] and optical-fiber interferometric temperature sensors [3–7]. The temperature measurement range of a fiber grating is limited and, in the low-temperature region, its sensitivity is relatively low. Optical-fiber interferometric temperature sensors are mainly based on Fabry–Pérot interferometers (FPI) [3], Mach–Zehnder interferometers (MZI) [4], Michelson interferometers (MI) [5], and Sagnac interferometers (SI) [6, 7]. Optical-fiber interferometric temperature sensors have been widely used in communication, construction industry, aerospace, and scientific research. However, these applications are strongly limited by the sensitivity and linearity of the sensor, which are governed by the intrinsic structural properties of the sensors.

One of the effective methods to improve the sensitivity of the instrument measurement is the employment of the Vernier effect, which is widely used in calipers and barometers. In recent years, fiber sensors with enhanced sensitivity based on the Vernier effect have been proposed to measure strain [8], hydrogen concentration [9], refractive index [10], gas pressure [11], and temperature [12]. Concerning the Vernier-effect-based devices, much attention has been paid to high-sensitivity temperature sensors, such as two cascaded MZIs [13], cascaded MI structure [14], two cascaded SIs [15, 16], cascaded SI and

Manuscript submitted by the authors in English on August 16, 2021.

FPI [17], as well as cascaded SI and MZI [18]. In particular, the FPI-based Vernier-effect temperature sensor has been in focus [19–22]. Gomes et al. reported a multimode FPI probe and the Vernier effect to enhance the temperature sensitivity to −654 pm/°C [19]. Zhang et al. employed a hollow fiber and a single-mode fiber to form an FPI and produce the Vernier effect to improve the temperature sensitivity to 1.019 nm/°C [20]. Yang et al. proposed the sensor based on cascaded FPIs, involving a silica tube and a single-mode fiber to produce the Vernier effect, which enhanced the temperature sensitivity to 183.99 pm/°C [21]. Zhang et al. reported a high-temperature Vernier probe based on an FPI using a photonic-crystal fiber, with its temperature sensitivity reaching 535.16 pm/°C [22]. However, using the cascading method to obtain the Vernier-effect temperature sensor is not an easy task, and the sensitivity enhancement factor of such devices is not easy to adjust. Sometimes, the Vernier effect cannot be achieved in the prepared sensors.

In this paper, we present a novel FPI-based Vernier-effect temperature sensor. The sensor comprises two parallel FPIs consisting of a single-mode fiber inserted into a ceramic ferrule and an UV-curable glue film on the end surface of the ceramic ferrule. In our scheme, the sensing and reference cavities during the sensor manufacturing can be fabricated independently to effectively design various cavity shapes. The parallel structure is different from the cascaded structure, which prevents the reference cavity from being affected by the sensing environment and significantly improves the system stability. Our designed sensor can easily produce the Vernier effect, which can be an effective solution to the problem of preparing the Vernier-effect sensors. The temperature sensitivity of the proposed sensor reaches −14.633 nm/°C, which is 9.6 times that of the temperature sensors based on a single FPI. Our sensor has simple structure, good repeatability, high sensitivity, and low cost, showing an important application value in the market.

The outline of this paper is as follows.

In Sec. 2, we introduce the sensor structure and the operation principle. In Sec. 3, we present the experimental results on temperature sensing and the analysis. Finally, in Sec. 4, we provide the summary.

2. Sensor Structure and Operation Principle

In Fig. 1, we show the proposed sensor structure, which comprises the sensor FPI (FPI_1) and the reference FPI (FPI_2) coupled in parallel. A 3 dB coupler is used to connect a broadband light source (BBS), FPI_1, FPI_2, and an optical spectrum analyzer (OSA). The light emitted from the BBS is split into two paths through a 3 dB coupler and transmitted to FPI_1 and FPI_2. After two Fabry–Pérot (F–P) cavity reflections, the two beams return to the coupler and interfere, and the superimposed light is delivered to the OSA. If the beam reflection spectra have close FSR, the beams produce the Vernier effect when superimposed.

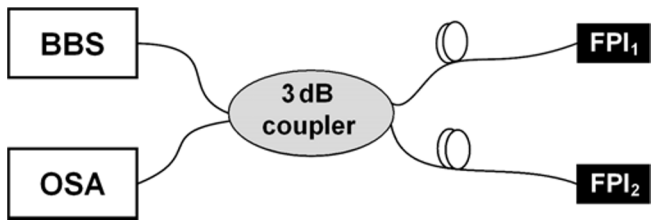

Fig. 1. Schematic diagram of the sensor composed of FPI_1 and FPI_2 coupled in parallel.

In Fig. 2, we show a schematic diagram of the structures of FPI_1 and FPI_2; they consist of a single-mode fiber inserted into a ceramic ferrule and an UV-curable glue film on the end surface of the ceramic ferrule. In our structure, FPI_1 (sensing element) and FPI_2 (reference element) can be fabricated independently, and the difference in the cavity lengths for the two FPIs (L_1 and L_2) can be accurately tailored, yielding a large and well-controlled enhancement factor, when using the Vernier effect. By analyzing the drift characteristics of the envelope extracted from the reflection spectrum of the sensor, high temperature

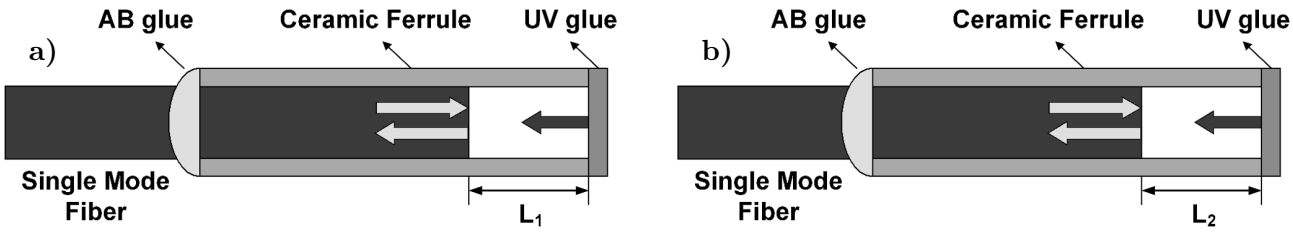

Fig. 2. Structure schematic diagram for FPI_1 (a) and FPI_2 (b).

sensitivity of the sensor can be achieved.

During the FPI manufacturing process, the OSA can be used to monitor the real-time reflection spectrum of the FPI structure. Therefore, the FSR of the two FPIs can be accurately determined when the cavity length of the FPIs is determined. The relationship between the cavity length and the FSR of FPIs is as follows:

$$\mathrm{FSR} = \frac{\lambda^2}{2n_{\mathrm{air}}L}, \tag{1}$$

where λ is the wavelength of the incident light, L is the cavity length, and n_{air} is the refractive index (RI) of air in the F–P cavity ($n_{\mathrm{air}} \approx 1$). Finally, in Fig. 3, we show the reflection spectra of two separate FPIs, where one can see that the FSR values of FPI_1 and FPI_2 are ∼8 and ∼7.2 nm, respectively. It is inconvenient to measure the length of the FPIs using a microscope for this sensor, so we used formula (1) to theoretically determine the cavity lengths of FPI_1 and FPI_2 for further calculations, which are ∼150 and ∼167 μm, respectively. In the subsequent temperature sensing tests of single FPI_1, the Dip $_1$ (∼1532 nm) was used as the tracking wavelength.

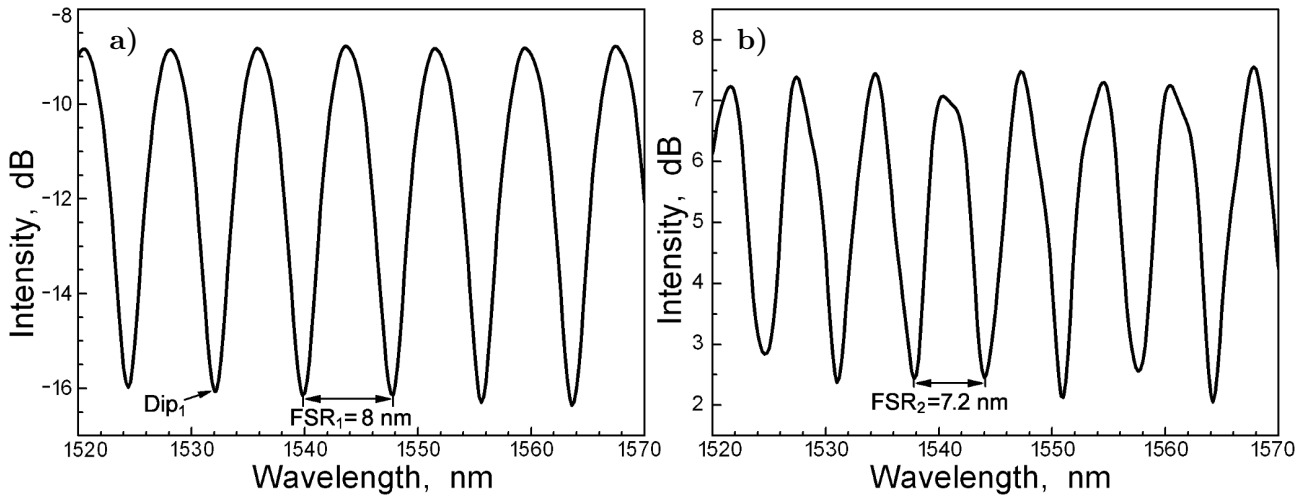

Fig. 3. Reflection spectra of FPI_1 (a) and FPI_2 (b) at 50°C.

In Fig. 4, we present the output spectrum of the sensor, which comprises a high-frequency interference fringe and a slowly varying envelope. The high-frequency oscillation is similar to the spectrum of FPI_1 or FPI_2, and the envelope is determined by the FSR difference for the two FPIs. To better track the envelope peak drift and enhance the measurement sensitivity of the sensor, the envelope lines can be gained, using known curves. In the subsequent temperature sensing tests, the lower envelope $Peak_1$

(∼1528 nm) was used as the tracking wavelength.

In the sensor, all reflections are due to Fresnel reflection from the silicon–air interface or the air–UV-curable-glue-film interface. However, due to the relatively small reflectivity of the interfaces, only part of the power will be reflected, while a large part of the power will be transmitted. Meanwhile, owing to the air cavity and light transmission in free space, the transmission loss and coupling loss between the SMF and the UV-curable glue film are large. Thus, multibeam interference can be ignored for both FPIs, and they can be considered as two-beam interferometers. The resonance modes of the two F–P cavities determine the reflection spectrum, wherein the case of two parallel FPIs can be described as

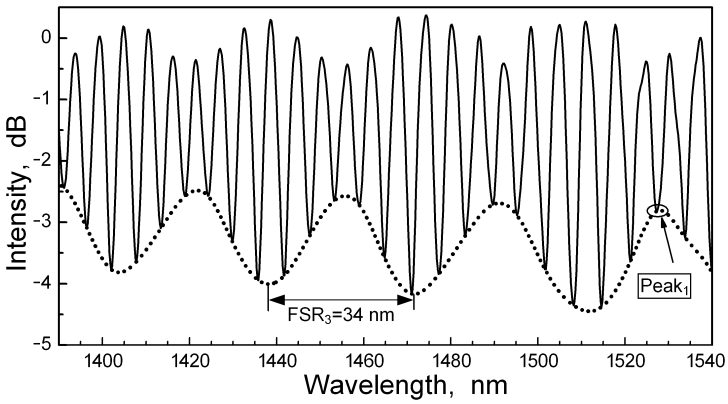

Fig. 4. Reflection spectrum of the proposed sensor including high-frequency interference fringes (the solid curve) and a lower-frequency envelope (the dotted curve) at $T = 56°\mathrm{C}$.

$$I = I_1 + I_2 + I_3 + I_4 + 2\sqrt{I_1 I_2}\cos(4\pi n_{\mathrm{air}} L_1/\lambda) + 2\sqrt{I_3 I_4}\cos(4\pi n_{\mathrm{air}} L_2/\lambda). \tag{2}$$

Here, I is the total light intensity, I_1, I_2, I_3, and I_4 are the intensities of the light reflected by the four reflective surfaces of FPI_1 and FPI_2, respectively, L_1 and L_2 are the cavity lengths of FPI_1 and FPI_2, respectively, n_{air} is the refractive index (RI) of air in the two FPIs, and λ is the wavelength of light in free space.

First, we analyze the temperature response of a single FPI_1. The wavelength λ_m of the m_{th} interference dip of FPI_1 can be calculated as

$$\lambda_m = \frac{4L_1 n_{\mathrm{air}}}{2m+1}, \qquad m = 1, 2, 3\ldots \tag{3}$$

The UV-curable glue used in the sensor structure is NOA65; it has a high thermal expansion coefficient. With increasing the temperature, NOA65 expands rapidly, resulting in a reduced cavity length of FPI_1. Though the ambient temperature also affects the effective RI of air in the F–P cavity and the length of the ceramic ferrule, the corresponding change is so small that it can be neglected. Therefore, as for the FPI_1 temperature sensor, its sensitivity S_{T_1} is calculated as [23]

$$S_{T_1} = \frac{d\lambda_m}{dT} = \lambda_m\left(\frac{1}{L}\frac{dL}{dT} + \frac{1}{n_{\mathrm{air}}}\frac{dn_{\mathrm{air}}}{dT}\right) \approx \lambda\cdot\alpha, \qquad m = 1, 2, 3, \ldots, \tag{4}$$

where T is the ambient temperature, and α is the thermal expansion coefficient of NOA65 equal to $220\cdot 10^{-6}/°\mathrm{C}$ [23]. Due to the large thermal expansion coefficient of NOA65, the temperature sensitivity of FPI_1 is high.

To further enhance the temperature sensitivity, FPI_1 was connected with FPI_2 in parallel to obtain the Vernier effect. According to the interference theory, the FSR of the reflection spectrum envelope is much larger than that of a single FPI and is defined as [19]

$$\mathrm{FSR}_{\mathrm{envelope}} = \frac{\mathrm{FSR}_1\cdot\mathrm{FSR}_2}{|\mathrm{FSR}_1 - \mathrm{FSR}_2|}. \tag{5}$$

In the Vernier-effect sensor elaborated, FPI_1 plays a sensing role, and FPI_2 acts as a reference. Therefore, when the temperature changes, the wavelength of FPI_1 will drift, causing the enhancement of the wavelength drift of the envelope by a factor of M, which is expressed by the following formula [20, 21]:

$$M = \frac{\mathrm{FSR}_{\mathrm{envelope}}}{\mathrm{FSR}_1} = \frac{L_1}{|L_2 - L_1|}. \tag{6}$$

It is seen in Eq. (6) that M depends only on the cavity lengths of the two FPIs. Thus, in device manufacturing, precise control of the F–P cavity length ensures that the enhancement factor reaches the expected value. In addition, the smaller the cavity length difference for FPI_1 and FPI_2, the greater the enhancement factor obtained. However, if the cavity length difference is too small, the envelope FSR becomes very large, which may lead to an envelope drift beyond the BBS wavelength range, making the measurement difficult to perform. According to the Vernier effect, the envelope drift ($\Delta\lambda_{\mathrm{envelope}}$) of the reflection spectrum of the proposed sensor is M times the wavelength shift ($\Delta\lambda$) of FPI_1. Thus, the temperature sensitivity of the proposed sensor is M times that of the single FPI_1 sensor. The sensitivity enhancement corresponds to the Vernier effect, which is the theoretical basis for our proposed structure implementation for high-sensitivity temperature detection. The temperature sensitivity of the envelope of the proposed sensor can be described as

$$S_{T_{\mathrm{envelope}}} = M \cdot S_{T_1}. \tag{7}$$

3. Experimental Setup

The experimental device for temperature sensing using the parallel-structure sensor is shown in Fig. 5. A 3 dB fiber coupler was employed to connect the BBS (FL-ASE-EB-D-2-2-FC/APC, Beijing, China), OSA (Yokogawa, AQ6370D), FPI_1, and FPI_2, and only FPI_1 was placed in a programmable temperature and humidity test box (WHTH-80L-0-OYO, Dongguan, China) with a temperature measurement accuracy of ±0.1°C. During the experiment with the parallel-structure sensor, the temperature was varied from 56°C to 68°C with a step of 3°C. After each temperature change, we waited for 5 min to ensure that the system reached thermal equilibrium before recording the data. At the same time, in the experiment with the single FPI_1, FPI_2 is not needed to be connected to the 3 dB coupler, and the temperature increases from 50°C to 80°C with a step of 5°C.

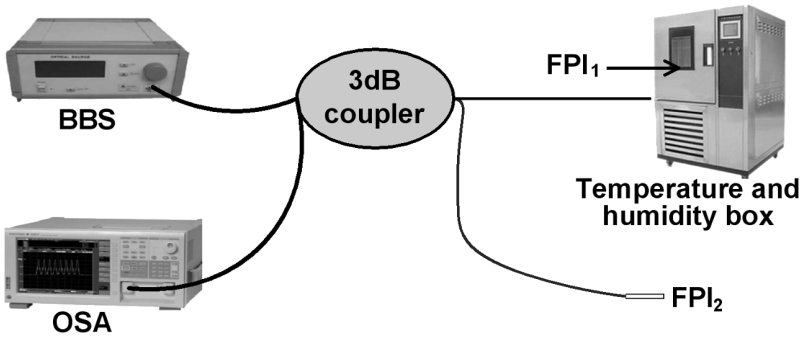

Fig. 5. Experimental setup for the temperature measurement by the sensor.

4. Experimental Results and Discussion

4.1. Temperature Sensitivity

The shifts of the lower envelope Peak_1 in the sensor reflection spectrum are shown in Fig. 6 a, with the temperature increasing from 56°C to 68°C. It can be found that the spectral envelope for the sensor

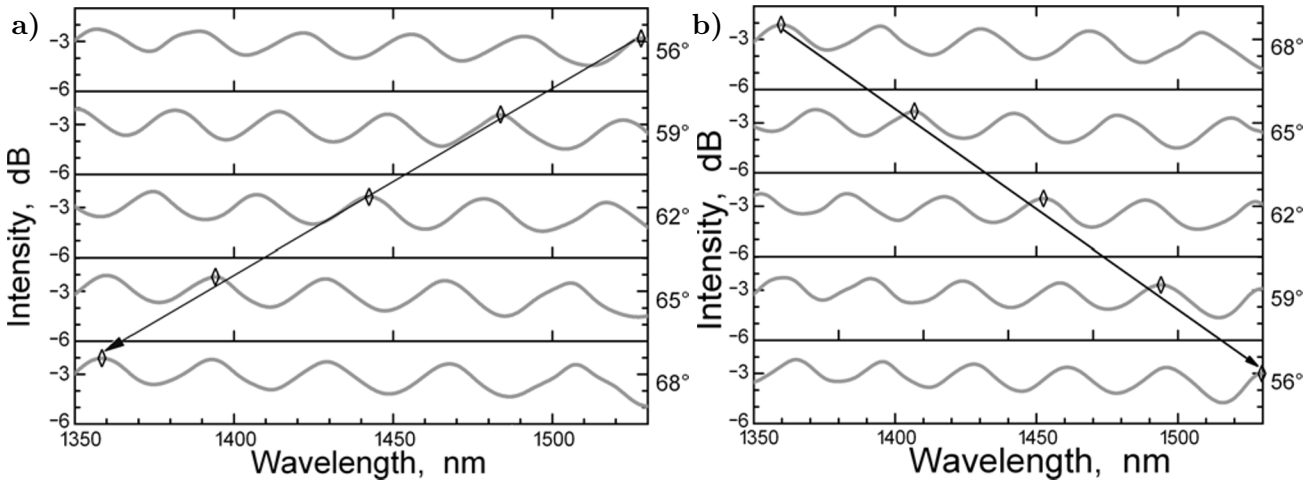

Fig. 6. Shifts of the lower envelope Peak_1 with temperature, namely, increase from 56°C to 68°C (a) and decrease from 68°C to 56°C (b).

has a large blue shift (∼175 nm) as the temperature increases. Figure 6 b shows the shifts of the lower envelope Peak_1 with the temperature decreasing from 68°C to 56°C. The spectral envelope for the sensor has a large red shift (∼166 nm), following the decrease in temperature.

In Fig. 7, we show the fits of the shifts of the lower envelope Peak_1 with increase and decrease in the temperature. It can be seen that, as the temperature increases from 56°C to 68°C, the lower envelope Peak_1 linearly shifts to shorter wavelengths, and we obtain a temperature sensitivity of −14.633 nm/°C with a linear scale factor of 99.83%. Also, as the temperature decreases from 68°C to 56°C, the lower envelope Peak_1 linearly shifts to longer wavelengths, and we obtain the temperature sensitivity of −13.82 nm/°C with a linear scale factor of 99.58%. Thus, the temperature sensitivity of the sensor is almost unchanged when the temperature rises or drops. The sensor has a small hysteresis error. The sensitivity of the proposed sensor is higher than that found in the literature [19–22] or comparable to the published data [23].

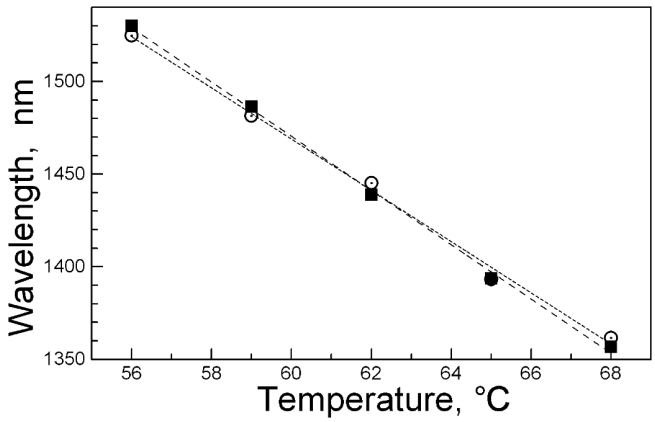

Fig. 7. Fits of the shifts of the lower envelope Peak_1 with increasing (■) and decreasing (⊙) temperatures.

Figure 8 shows the shifts for the single FPI_1 with increase in the temperature, which indicates that Dip_1 wavelength of the FPI_1 spectrum has a red shift (∼46 nm) with the temperature increasing from 50°C to 80°C. The fit of the wavelength shifts for Dip_1 with changing temperature is shown in Fig. 9, which gives the temperature sensitivity of 1.5271 nm/°C with a linear scale factor of 99.29%. By comparing the temperature sensitivity for the lower envelope Peak_1 and that of the single FPI_1, we obtain the experimental sensitivity enhancement factor of 9.6 (14.633/1.5271 = 9.6), which shows an obviously enhanced temperature sensitivity, meaning a notable Vernier effect. Such sensitivity enhancement factor is basically consistent with the theoretically calculated value, $M = \dfrac{L_1}{|L_2 - L_1|} = 8.8$. The minor difference

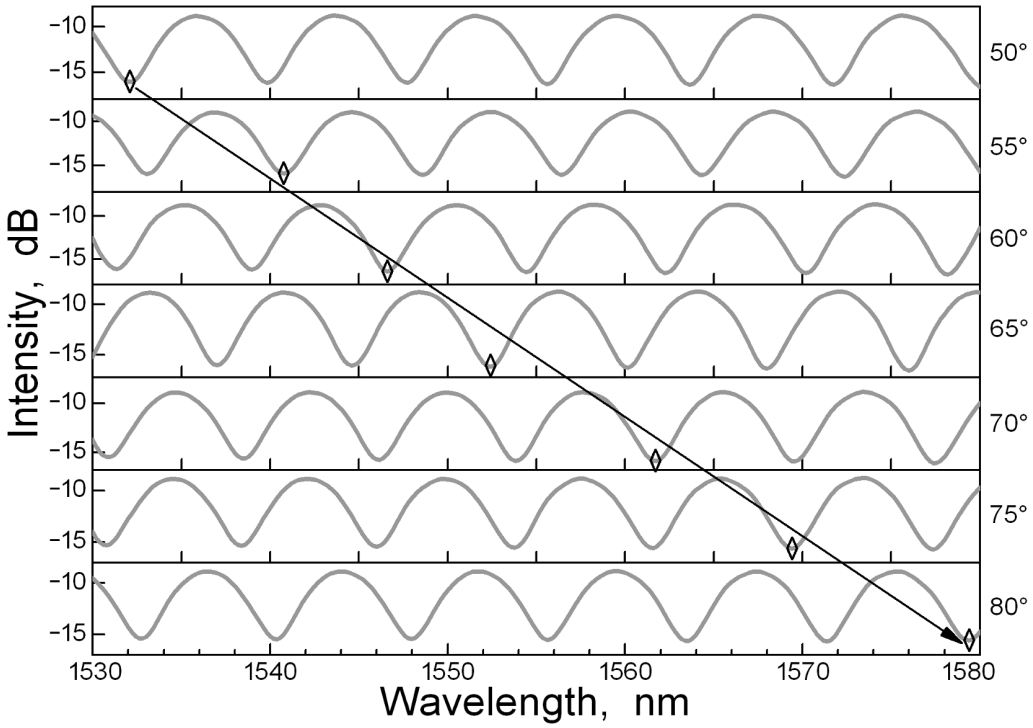

Fig. 8. Shifts for the single FPI_1 with the temperature increasing from 50°C to 80°C.

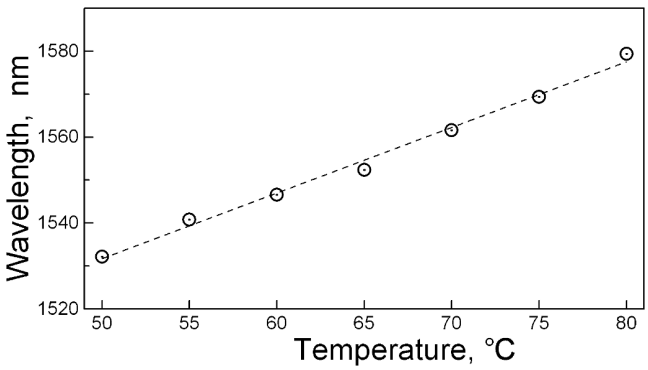

Fig. 9. Fit of the wavelength shifts for the single FPI_1 with changing temperature.

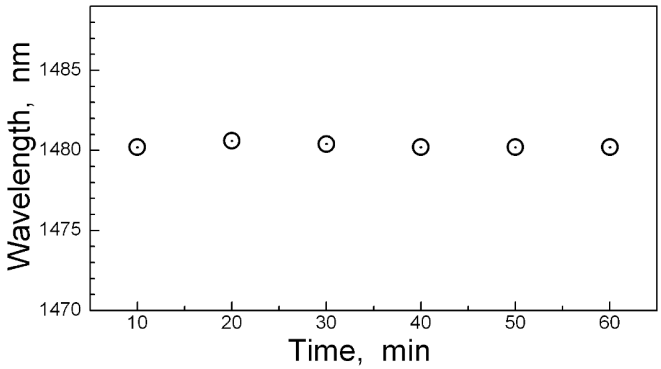

Fig. 10. Temperature measurement stability of the sensor at $T = 60°$.

between the experimental result and theoretically calculated value is mainly due to the fact that the wavelength of the selected $Peak_1$ and Dip_1 is not exactly 1550 nm.

4.2. Stability Experiment

The measurement error of the sensor was investigated through stability experiments. In the stability experiment, the sensor was placed in the temperature box for long-term testing at a constant temperature 60°C. In Fig. 10, we show the experimental results on the wavelength response of the lower envelope $Peak_1$ (1480.3 nm) over the 60 min time range. The peak wavelength reveals almost no change, which shows

that the sensor elaborated has good stability. The maximum wavelength shift of the lower envelope $Peak_1$ is 0.3 nm. Thus, the measurement error of the proposed sensor is estimated to be about 0.02°C (0.3/14.633 = 0.02°C). The error of the temperature is within the permitted range, which demonstrates that the sensor has a good measurement accuracy.

4.3. Repeatability Experiment

To test the repeatability of the proposed sensor, we performed three temperature experiments for the sensor after long-time intervals. In Fig. 11, we present the experimental results of three temperature measurements, which show that the temperature sensitivity in the three measurements has the same value of −14.073 nm/°C. The experimental results reveal that the measured deviation is rather small, and the data obtained in the three experiments are basically consistent. Therefore, the sensor is demonstrated to have good repeatability.

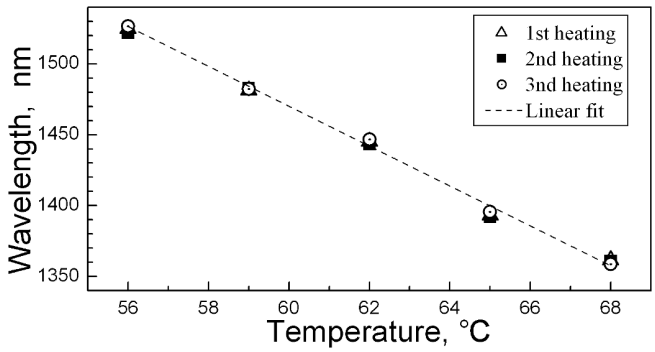

Fig. 11. Experimental results of three temperature measurements shown by △, ■ and ⊙ for the sensor with increasing temperature.

5. Conclusions

In this study, we presented a novel FPI-based Vernier-effect temperature sensor. The sensor comprises two parallel FPIs (FPI_1 and FPI_2), which consist of a single-mode fiber inserted into a ceramic ferrule and a UV-curable glue film on the end surface of the ceramic ferrule. In the sensor, FPI_1 acts as a sensing element, and FPI_2 plays a role of a reference element. The proposed sensor can easily produce the Vernier effect, which can effectively reduce the fabrication difficulty of Vernier-effect sensors. The experimental results show that the temperature sensitivity of the sensor elaborated reaches −14.633 nm/°C, which is 9.6 times that of the single FPI_1 temperature sensor. The designed sensor will have wide application prospects due to its simple structure, good repeatability and stability, high sensitivity, and low cost.

Acknowledgments

The authors acknowledge the financial support provided within the Natural Science Foundation of Hubei Province under Project No. 2020CFB46 and the Middle-aged and Youth Science and Technology Innovation Team of Hubei Province Universities under Project No. T2020014.

References

1. Y. P. Wang, W. Jin, D. N. Wang, et al., *Opt. Lasers Eng.*, **47**, 1044 (2009).
2. K Chah, K. Yuksel, D Kinet, et al., *Opt. Lett.*, **44**, 4036 (2019).
3. F. Z. Zhang, N. Zhao, Q. J. Lin, et al., *AIP Adv.*, **10**, 085118 (2020).
4. S. N. Wang, R. Q. Lv, Y. Zhao, et al., *Opt. Fiber Technol.*, **45**, 93 (2018).
5. Y. Han, B. Liu, Y. F. Wu, et al., *Opt. Express*, **29**, 6703 (2021).
6. L. Shao, J. Hu, H. Lu, et al., *Photonic Sens.*, **9**, 25 (2019).

7. M. Ma, H. Chen, S. Li, et al., *Optik*, **179**, 665 (2019).
8. T. Nan, B. Liu, Y. F. Wu, et al., *Opt. Express*, **27**, 17239 (2019).
9. Y. Li, C. Zhao, B. Xu, et al., *Opt. Commun.*, **414**, 166 (2018).
10. B. Troia, F. D. Leonardis, and V. M. N. Passaro, *Sens. Actuators B*, **240**, 76 (2017).
11. Q. H. Wang, X. Liu, and D. N. Wang, *Opt. Fiber Technol.*, **61**, 102404 (2021).
12. Y. B. Ying, C. L. Zhao, H. P. Gong, et al., *Opt. Laser Technol.*, **118**, 126 (2019).
13. Z. R. Wang, L. Huang, C. Liu, et al., *IEEE Sens. J.*, **19**, 7983 (2019).
14. Y. Zhao, M. Dai, Z. Chen, et al., *Opt. Express*, **29**, 1090 (2021).
15. Q. Liu, L. Xing, S. Yan, et al., *Metrologia*, **57**, 35002 (2020).
16. Z. Ding, Z. Tan, P. Zhang, et al., *J. Opt. Soc. Am. B*, **37**, 1948 (2020).
17. Y. Yang, Y. Wang, Y. Zhao, et al., *Opt. Express*, **25**, 33290 (2017).
18. X. Jia, X. Zhou, M. Bi, et al., *Opt. Fiber Technol.*, **65**, 102625 (2021).
19. A. D. Gomes, M. Becker, J. Dellith, et al., *Sensors*, **19**, 453 (2019).
20. P. Zhang, M. Tang, F. Gao, et al., *IEEE Photonics J.*, **7**, 7100210 (2015).
21. Y. Yang, Y. Wang, Y. Zhao, et al., *J. Russ. Laser Res.*, **40**, 243 (2019).
22. G. Zhang, X. Q. Wu, W. J. Zhang, et al., *Opt. Express,* **27**, 37308 (2019).
23. J. Zhang, H. Liao, P. Lu, et al., *IEEE Photonics J.*, **10**, 6803411(2018).